

HI intensity mapping with MeerKAT: power spectrum detection in cross-correlation with WiggleZ galaxies

Steven Cunnington¹,^{1,2}★ Yichao Li,^{3,4} Mario G. Santos,^{4,5} Jingying Wang¹,^{4,6} Isabella P. Carucci,^{7,8} Melis O. Irfan,^{4,9} Alkistis Pourtsidou,^{2,4,10} Marta Spinelli¹,^{4,11} Laura Wolz,¹ Paula S. Soares¹,⁹ Chris Blake,¹² Philip Bull,^{4,9} Brandon Engelbrecht,⁴ José Fonseca¹,¹³ Keith Grainge¹ and Yin-Zhe Ma^{14,15}

¹Jodrell Bank Centre for Astrophysics, Department of Physics & Astronomy, The University of Manchester, Manchester M13 9PL, UK

²Institute for Astronomy, The University of Edinburgh, Royal Observatory, Edinburgh EH9 3HJ, UK

³Department of Physics, College of Sciences, Northeastern University, Wenhua Road, Shenyang, 11089, China

⁴Department of Physics and Astronomy, University of the Western Cape, Robert Sobukwe Road, Cape Town, 7535, South Africa

⁵South African Radio Astronomy Observatory (SARAO), 2 Fir Street, Cape Town, 7925, South Africa

⁶Shanghai Astronomical Observatory, Chinese Academy of Sciences, 80 Nandan Road, Shanghai, 200030, China

⁷Dipartimento di Fisica, Università degli Studi di Torino, via P. Giuria 1, I-10125, Torino, Italy

⁸INFN - Istituto Nazionale di Fisica Nucleare, Sezione di Torino, via P. Giuria 1, I-10125, Torino, Italy

⁹Department of Physics & Astronomy, Queen Mary University of London, London, E1 4NS, UK

¹⁰Higgs Centre for Theoretical Physics, School of Physics and Astronomy, The University of Edinburgh, Edinburgh EH9 3FD, UK

¹¹Institute of Particle Physics & Astrophysics, Department of Physics, ETH Zurich, 8093 Zurich, Switzerland

¹²Centre for Astrophysics & Supercomputing, Swinburne University of Technology, PO Box 218, Hawthorn, VIC 3122, Australia

¹³Instituto de Astrofísica e Ciências do Espaço, Universidade do Porto CAUP, Rua das Estrelas, PT4150-762 Porto, Portugal

¹⁴NAOC-UKZN Computational Astrophysics Center (NUCAC), University of Kwazulu-Natal, Durban, 4000, South Africa

¹⁵School of Chemistry and Physics, University of KwaZulu-Natal, Westville Campus, Private Bag X54001, Durban, South Africa

Accepted 2022 October 20. Received 2022 October 20; in original form 2022 June 3

ABSTRACT

We present a detection of correlated clustering between *MeerKAT* radio intensity maps and galaxies from the WiggleZ Dark Energy Survey. We find a 7.7σ detection of the cross-correlation power spectrum, the amplitude of which is proportional to the product of the HI density fraction (Ω_{HI}), HI bias (b_{HI}), and the cross-correlation coefficient (r). We therefore obtain the constraint $\Omega_{\text{HI}}b_{\text{HI}}r = [0.86 \pm 0.10 (\text{stat}) \pm 0.12 (\text{sys})] \times 10^{-3}$, at an effective scale of $k_{\text{eff}} \sim 0.13 h \text{ Mpc}^{-1}$. The intensity maps were obtained from a pilot survey with the *MeerKAT* telescope, a 64-dish pathfinder array to the SKA Observatory (SKAO). The data were collected from 10.5 h of observations using *MeerKAT*'s L-band receivers over six nights covering the 11 h field of WiggleZ, in the frequency range 1015–973 MHz ($0.400 < z < 0.459$ in redshift). This detection is the first practical demonstration of the multidish autocorrelation intensity mapping technique for cosmology. This marks an important milestone in the roadmap for the cosmology science case with the full SKAO.

Key words: (*cosmology*;) large-scale structure of Universe – cosmology: observations – methods: data analysis – methods: statistical – radio lines: general.

1 INTRODUCTION

Probing the large-scale structure of the Universe is a crucial step towards precision cosmology as we try to constrain the nature of dark energy, non-Gaussian fluctuations in the Universe's primordial density field, and test general relativity. Typically, this is done using galaxy surveys with spectroscopic or photometric redshifts in the optical or near-infrared. At radio wavelengths, we use the redshifted neutral hydrogen (HI) hyperfine transition line, with a rest-frame wavelength of 21 cm, to measure redshift. Given the ubiquitous

nature of HI in the Universe, we can use it to trace the distribution of dark matter at low and high redshifts.

The faintness of the HI emission line makes it challenging to resolve individual galaxies at higher redshifts over large volumes. However, for cosmology we are interested in the bulk fluctuations on large (Mpc) scales, so we can use the HI intensity mapping technique. This technique relaxes the requirement of galaxy detection by integrating all 21 cm emission within relatively large spatial voxels (Bharadwaj et al. 2001; Battye, Davies & Weller 2004; Chang et al. 2008; Wyithe, Loeb & Geil 2008). This delivers high survey speeds over large volumes, providing a novel solution to the current challenges of observational cosmology.

One of the main challenges in detecting the HI intensity mapping signal is the presence of foregrounds that are orders of magnitude

* E-mail: steven.cunnington@manchester.ac.uk

brighter. Removing these requires precise instrumental calibration. Cross-correlating with galaxy surveys helps to mitigate residual systematics from foregrounds, radio frequency interference (RFI), and thermal noise (Wolz et al. 2016; Pourtsidou, Bacon & Crittenden 2017). Moreover, it can improve constraints on cosmological parameters and provide insight into the H I astrophysics of the correlated galaxies (Anderson et al. 2018; Wolz et al. 2022, hereafter W22). A number of forthcoming telescopes are aiming to conduct H I intensity mapping surveys, such as CHIME (Newburgh et al. 2014), uGMRT (Chakraborty et al. 2021), Tianlai (Li et al. 2020), HIRAX (Newburgh et al. 2016), CHORD (Vanderlinde et al. 2019), and PUMA (PUMA Collaboration et al. 2019), all of which are interferometers. There are also individual single-dish receivers such as FAST (Bigot-Sazy et al. 2016) and BINGO (Wuensche 2019). Currently, the H I intensity mapping signal has only been detected in cross-correlation with galaxy surveys (Chang et al. 2010; Masui et al. 2013; Anderson et al. 2018; Tramonte & Ma 2020; Li, Staveley-Smith & Rhee 2021a; CHIME Collaboration et al. 2022; W22).

Both MeerKAT and the future SKA Observatory (SKAO) have been put forward as state-of-the-art intensity mapping instruments capable of complementing and extending cosmological measurements at other wavelengths (Santos et al. 2017; SKA Cosmology SWG 2020). Using the single-dish data from each element of the array (Battye et al. 2013; Bull et al. 2015), we can access the large cosmological scales inaccessible by the interferometer due to its lack of very short baselines.

In this article, we used data from a MeerKAT pilot survey to measure the cross-correlation power spectrum between the H I signal and overlapping WiggleZ data (Drinkwater et al. 2010). With only 10.5 h of data for each of the 64 dishes over an effective survey area of $\sim 200 \text{ deg}^2$, this detection shows the power of this approach and paves the way towards probing large cosmological scales with much larger surveys with MeerKAT and SKAO.

The paper is structured as follows: In Section 2, we introduce the data products used in this study. The formalism adopted for the power spectrum estimation and modelling is discussed in Section 3. Section 4 introduces our approach to foreground cleaning in the MeerKAT intensity maps. We present our main results in Section 5 and finally conclude in Section 6.

2 MEERKAT PILOT SURVEY DATA

Here, we summarize the MeerKAT instrument along with the observation strategy and pipeline used for obtaining the intensity mapping pilot survey data. The observational details are presented in Wang et al. (2021; hereafter W21) which describes in detail the calibration strategy and first sky maps analysis.

MeerKAT is based in the Upper Karoo region of South Africa and will eventually become a part of the final SKA1-Mid.¹ The SKAO is expected to end construction in 2029 July, meaning MeerKAT will be used up to then to deliver transformative science (Santos et al. 2017). MeerKAT is composed of 64 dishes, each of which is 13.5 m in diameter and can use three possible receivers, UHF band (580–1015 MHz), L band (900–1670 MHz), and S band (1750–3500 MHz). For the single-dish H I intensity mapping pilot survey data in this work the L-band receiver was used, in principle allowing $z < 0.58$ redshifts to be probed; however, we only use a small subset of this range as discussed later in this section.

For single-dish observations, we require a scanning strategy where the dishes are moved rapidly across the sky, covering a certain target patch. The survey targeted a single patch of $\sim 200 \text{ deg}^2$ in the WiggleZ 11 h field, covering $153^\circ < \text{R.A.} < 172^\circ$ and $-1^\circ < \text{Dec.} < 8^\circ$ (Blake et al. 2010; Drinkwater et al. 2010, 2018), avoiding the strongest region of Galactic emission. The observations took place over six nights between 2019 February and July, which allowed all observing to be done at high elevation ($>40 \text{ deg}$) to minimize fluctuations of ground spill and airmass. After accounting for calibration in the observations, each complete scan across the sky patch took around 1.5 h and we repeated this seven times over the six nights to give the 10.5 h of combined data. We refer to each 1.5 h scan as a *time block*. The 10.5 h of observational data is obtained for each of the 64 dishes, although data from ~ 4 dishes on average were completely removed from each time block due to equipment issues. The telescope scan speed (5 arcmin s^{-1} along azimuth) meant the dishes moved rapidly across the sky allowing 10 deg to be scanned in $\sim 100 \text{ s}$.

Our calibration strategy for the time-ordered data (TOD) involved the use of noise diodes which were fired every 20 s. Bandpass and absolute calibration of the diodes into Kelvin are performed through observation of a bright source of known flux density and spectrum. We use 3C 273 as a bright source calibrator for five of the seven time blocks, using 3C 237 and Pictor A for the remaining blocks. These diode solutions are then used to calibrate the TOD together with a multicomponent model. The use of the diode removes long-term noise correlation, so-called $1/f$ noise, due to receiver chain gain variations on time-scales longer than 20 s. On shorter time-scales, $1/f$ noise is negligible compared to thermal noise fluctuations (Li et al. 2021b). We also subtract the average signal every 220 s in the TOD which suppresses residual very long time-scale gain changes. This should reduce the overall variance of the signal but can potentially have the adverse effect of removing H I signal over large angular scales. In this work, we assume any signal loss from this process is subdominant relative to the signal loss from foreground cleaning and thus do not attempt any reconstruction.

The data underwent three levels of RFI flagging at different stages of the calibration, starting with strong RFI flagging on the raw signal using the SEEK package (Akeret et al. 2017), then removing per-channel outliers in the TOD, then finally removing residual low-level RFI features, later in the pipeline after the map-making. Since these were dual-polarization autocorrelation observations, each dish and time block provide separate HH and VV polarization data at each frequency in the L band. The mean-value of the two calibrated polarization temperatures gives the total intensity corresponding to the Stokes I. At each frequency and time block, the TOD for each dish, d , is projected into the map space via the map-making process (Tegmark 1997):

$$\hat{m} = (A^T N^{-1} A)^{-1} A^T N^{-1} d, \quad (1)$$

in which A is the pointing matrix mapping the TOD to the map coordinates and N is the noise covariance matrix between time stamps.

The noise covariance matrix N is assumed to be diagonal with constant variance during the observation; however, we allow the variance to differ between dishes. The noise covariance is also projected to the map space via:

$$\hat{n} = (A^T N^{-1} A)^{-1}, \quad (2)$$

where \hat{n} is the pixel noise variance. The inverse of the pixel noise variance, $w_{\text{H I}} = 1/\hat{n}$, is used as the inverse-variance weight in the

¹<https://www.skao.int/>

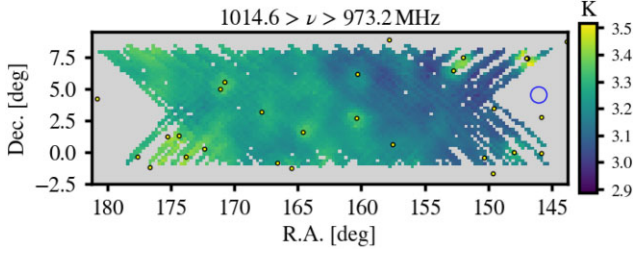


Figure 1. *MeerKAT* intensity map showing the total sky in the WiggleZ 11 h field, which is dominated by foreground emission. The map has been averaged over the 199 frequency channels covering 1014.6 > ν > 973.2 MHz ($0.400 < z < 0.459$). The yellow dots show the position of point sources with flux > 1 Jy at 1400 MHz. The blue ring shows the full width at half-maximum (FWHM) of the *MeerKAT* beam at the mean frequency.

analysis.² We use the flat-sky approximation and grid the maps into square pixels with a width of 0.25 deg. To create the final maps, we average over all individual dish maps and time blocks at each frequency.

The *MeerKAT* *L* band has 4096 frequency channels; however, in this work, we only use 199 channels at 973.2–1014.6 MHz ($0.400 < z < 0.459$). Whilst using more frequency channels would in principle improve signal-to-noise (S/N) in the cross-correlation, since there are WiggleZ galaxies available beyond these redshifts, we find the data to be more RFI dominated outside these frequency ranges, and flagging them is the safest option initially. Of the 199 channels selected to use, a further 32 are removed due to their dominant contributions to the eigenmodes of the principal component analysis (PCA; see later discussion in Section 4) for those particular channels. This aggressive strategy can be seen as a final RFI-flagging stage and was necessary in order for us to obtain a cross-correlation detection. We leave to future work an investigation into a less aggressive flagging approach to see if this is beneficial in more sophisticated foreground cleaning algorithms. The observed map showing the total sky dominated by the foregrounds is shown in Fig. 1. This shows good agreement with models of diffuse Galactic emission (see comparison in W21) and a correlation can be seen by eye between the observed emission and the position of known point sources (obtained from the NED³ data set), indicated by the yellow dots.

The *MeerKAT* dish-diameter of 13.5 m creates a large beam when used in single-dish mode. The FWHM of the central lobe for the beam can be given approximately by $\theta_{\text{FWHM}} = 1.16 c\nu/D_{\text{dish}}$ (Matshawule et al. 2021), where c is the speed of light, ν is the frequency of observation, and D_{dish} is the dish diameter. For the *MeerKAT* pilot survey this gives $\theta_{\text{FWHM}} = 1.48$ deg at the mean frequency. This size of the beam is demonstrated in Fig. 1 by the blue ring which shows good agreement with the approximate sizes of the strongest point sources.

3 POWER SPECTRUM ESTIMATION & MODELLING

Here we present the adopted formalism for the power spectrum estimation, along with the theoretical prediction used for comparison with the measurements. The power spectrum estimation process

²We adopt the HI in the subscript of w_{HI} to maintain a consistent notation with later formalism where the intensity maps weights require distinguishing from the galaxy weights.

³<http://ned.ipac.caltech.edu/byparams>

is based on the optimal weighting method outlined in Feldman, Kaiser & Peacock (1994; see Wolz et al. 2017 and Blake 2019 for applications to HI intensity mapping cross-correlations). We also discuss our approach to error estimation. The theoretical model fitted to the measured power spectrum is similar to previous studies (e.g. Masui et al. 2013; W22) whereby we use a biased matter power spectrum with a fixed cosmology, with some treatment to account for linear redshift-space distortions (RSDs) and damping from the telescope beam.

3.1 Power spectrum estimation

We begin by defining the two Fourier transformed fields of the HI temperature fluctuation maps δT_{HI} and the galaxy count field n_g as

$$\tilde{F}_{\text{HI}}(\mathbf{k}) = \sum_{\mathbf{x}} \delta T_{\text{HI}}(\mathbf{x}) w_{\text{HI}}(\mathbf{x}) \exp(i\mathbf{k} \cdot \mathbf{x}) \quad (3)$$

$$\tilde{F}_g(\mathbf{k}) = \sum_{\mathbf{x}} n_g(\mathbf{x}) w_g(\mathbf{x}) \exp(i\mathbf{k} \cdot \mathbf{x}) - N_g \tilde{W}_g(\mathbf{k}), \quad (4)$$

where $N_g = \sum_{\mathbf{x}} n_g$ is the total number of galaxies in the optical maps and \tilde{W}_g is the weighted Fourier transform of the selection function (W_g) which is normalized such that $\sum_{\mathbf{x}} W_g(\mathbf{x}) = 1$;

$$\tilde{W}_g(\mathbf{k}) = \sum_{\mathbf{x}} W_g(\mathbf{x}) w_g(\mathbf{x}) \exp(i\mathbf{k} \cdot \mathbf{x}). \quad (5)$$

The selection function W_g accounts for incompleteness in the WiggleZ survey and is constructed by stacking the random catalogues generated in Blake et al. (2010), reproducing the varying target and redshift completeness. The map weights in the above equations are the inverse-variance map for the HI field, $w_{\text{HI}}(\mathbf{x}) = 1/\hat{n}(\mathbf{x})$ (defined in Section 2), and for the galaxies we use the optimal weighting as per Feldman et al. (1994):

$$w_g(\mathbf{x}) = 1 / \left(1 + \frac{W_g(\mathbf{x}) N_g P_0}{V_{\text{cell}}} \right), \quad (6)$$

$$\hat{P}_{\text{HI},g}(\mathbf{k}) = \frac{V_{\text{cell}}}{\sum_{\mathbf{x}} w_{\text{HI}}(\mathbf{x}) w_g(\mathbf{x}) W_g(\mathbf{x})} \text{Re} \left\{ \tilde{F}_{\text{HI}}(\mathbf{k}) \cdot \tilde{F}_g^*(\mathbf{k}) \right\} \frac{1}{N_g}. \quad (7)$$

Similarly, the HI and galaxy autopower spectra, which are needed for the error estimation (see below), are given by

$$\hat{P}_{\text{HI}}(\mathbf{k}) = \frac{V_{\text{cell}}}{\sum_{\mathbf{x}} w_{\text{HI}}^2(\mathbf{x})} |\tilde{F}_{\text{HI}}(\mathbf{k})|^2, \quad (8)$$

$$\hat{P}_g(k) = \frac{V_{\text{cell}}}{\sum_{\mathbf{x}} w_g^2(\mathbf{x}) W_g^2(\mathbf{x})} [|\tilde{F}_g(\mathbf{k})|^2 - S_g] \frac{1}{N_g}, \quad (9)$$

where S_g accounts for the shot noise in the galaxy survey, given as

$$S_g = N_g \sum_{\mathbf{x}} w_g^2(\mathbf{x}) W_g(\mathbf{x}). \quad (10)$$

These power spectra are all spherically averaged into bandpowers $|\mathbf{k}| \equiv k$ to provide the final one-dimensional (1D) power spectra results. For noise-dominated HI intensity maps, the errors for the cross-power can be estimated analytically from

$$\hat{\sigma}_{\text{HI},g}(k) = \frac{1}{\sqrt{2N_m(k)}} \sqrt{\hat{P}_{\text{HI},g}^2(k) + \hat{P}_{\text{HI}}(k) \left(\hat{P}_g(k) + \frac{1}{\bar{n}_g} \right)}, \quad (11)$$

where N_m is the number of modes in each k -bin and $\bar{n}_g = N_g/(l_x \times l_y \times l_z)$ is the number density of galaxies. The $1/\sqrt{2}$ factor in equation (11) appears because this is the error on a cross-correlation of two fields, so the number of independent pairs available to measure the variance on the mean doubles. We compared these analytical error estimations to ones calculated from cross-correlating

the *MeerKAT* data with the random WiggleZ catalogues used to derive the selection function, finding very good agreement across all scales. Furthermore, we also found good agreement with an internal error estimation which used a jack-knife approach (Norberg et al. 2009).

3.2 Theoretical modelling

We fit a model to the cross-power spectrum which is given by

$$P_{\text{H1,g}}(\mathbf{k}) = \bar{T}_{\text{H1}} b_{\text{H1}} b_{\text{g}} r (1 + f\mu^2)^2 P_{\text{m}}(k) \times \exp\left[\frac{-(1 - \mu^2)k^2 R_{\text{beam}}^2}{2}\right], \quad (12)$$

where \bar{T}_{H1} is the mean H I temperature of the field in mK, b_{H1} and b_{g} are the H I and galaxy biases, and r is the cross-correlation coefficient. We account for linear RSDs with the $(1 + f\mu^2)^2$ factor (Kaiser 1987), where f is the growth rate of structure and μ is the cosine of the angle from the line-of-sight. P_{m} is the matter power spectrum produced using CAMB (Lewis, Challinor & Lasenby 2000) with a Planck18 (Planck Collaboration I 2020) cosmology. The exponential factor approximates the smoothing of perpendicular modes due to the *MeerKAT* beam, where R_{beam} is the standard deviation of the Gaussian beam profile in comoving units, taking into account the reconvolution (as later explained in Section 4.1), which gives $R_{\text{beam}} = 13.3 \text{ Mpc } h^{-1}$.

To fully account for RSD, the model in equation (12) should be (not including the beam damping for brevity)

$$P_{\text{H1,g}}(\mathbf{k}) = \bar{T}_{\text{H1}} [r b_{\text{H1}} b_{\text{g}} + b_{\text{H1}} f \mu^2 + b_{\text{g}} f \mu^2 + f^2 \mu^4] P_{\text{m}}(k), \quad (13)$$

which accounts for the biases appearing in cross-terms from the expansion of the two fields in redshift space $\delta_{\text{H1}}^s(\mathbf{k}) = b_{\text{H1}} \delta_{\text{m}}(\mathbf{k}) + f\mu \theta(\mathbf{k})$ and $\delta_{\text{g}}^s(\mathbf{k}) = b_{\text{g}} \delta_{\text{m}}(\mathbf{k}) + f\mu \theta(\mathbf{k})$, where $\theta(\mathbf{k})$ is the velocity divergence field.⁴ However, we are only attempting a fit to the spherically averaged power spectrum monopole, which is uniformly averaged across μ . This would make b_{H1} perfectly degenerate with $\bar{T}_{\text{H1}} r$. To break this degeneracy we would need to introduce an anisotropic sensitivity on μ in our analysis, achieved by modelling the quadrupole (Cunnington et al. 2020; Soares et al. 2021). This would require a higher S/N than we have available from the *MeerKAT* pilot survey data. This is why we follow previous literature (W22) and probe the degenerate quantity $\bar{T}_{\text{H1}} b_{\text{H1}} r$, but include a matter-only RSD, to avoid biasing the amplitude of the power spectrum by the $(1 + f\mu^2) \sim 1.7$ Kaiser term.

The model in equation (12) is discretized on to the same 3D grid of modes as the data and then convolved with the survey window functions:

$$P_{\text{H1,g}}(\mathbf{k}) \rightarrow P_{\text{H1,g}} * W_{\text{H1}} W_{\text{g}} = \frac{\sum_i P_{\text{H1,g}}(\mathbf{k}'_i) \text{Re} \{ \tilde{W}_{\text{g}}(\mathbf{k} - \mathbf{k}'_i) \tilde{W}_{\text{H1}}(\mathbf{k} - \mathbf{k}'_i)^* \}}{\sum_{\mathbf{x}} w_{\text{g}}(\mathbf{x}) w_{\text{H1}}(\mathbf{x}) W_{\text{g}}(\mathbf{x}) W_{\text{H1}}(\mathbf{x})}. \quad (14)$$

In lieu of a precisely constructed survey selection function W_{H1} for the H I intensity maps, we use a simple binary window function that is 1 wherever a pixel is filled and 0 otherwise. The convolved model in equation (14) is spherically averaged into the same k -bins as the data.

The mean H I temperature \bar{T}_{H1} can be recast to the H I density fraction (Ω_{H1}) using (Battye et al. 2013)

$$\bar{T}_{\text{H1}}(z) = 180 \Omega_{\text{H1}}(z) h \frac{(1+z)^2}{\sqrt{\Omega_{\text{m}}(1+z)^3 + \Omega_{\Lambda}}} \text{ mK}, \quad (15)$$

where Ω_{m} and Ω_{Λ} are the density fractions for matter and the cosmological constant, respectively. Thus fitting the amplitude of the cross-power spectrum allows us to constrain $\Omega_{\text{H1}} b_{\text{H1}} r$. When fitting $\Omega_{\text{H1}} b_{\text{H1}} r$ to the power spectrum data using the model in equation (12), we fix the galaxy bias (b_{g}) and growth rate (f), since they are well constrained from other experiments relative to the other parameters. We assume $f = 0.737$ [based on $f \sim \Omega_{\text{m}}(z)^\gamma$, where $\gamma = 0.545$ (Linder 2005; Planck Collaboration I 2020)] and $b_{\text{g}} = 0.911$ (Blake et al. 2011) at the central redshift of our data ($z_{\text{eff}} = 0.43$).

4 FOREGROUND CLEANING

Here, we discuss the foreground cleaning performed on the *MeerKAT* intensity maps. We provide detailed descriptions on each stage in the following subsections but begin with a summary of the foreground cleaning method we adopt.

Before cleaning, the maps are resmoothed using a Gaussian window function with kernel size 1.2 times the largest beam size within the frequency range (see Section 4.1 for details). The foreground cleaning is then performed using a blind PCA method, which relies on the foregrounds being the dominant signal and correlated in frequency. Thus, by removing the first N_{fg} principal component modes in frequency from each pixel, the majority of their contribution is suppressed (see Section 4.2 for further discussion). Foreground cleaning is imperfect, and the cleaned maps contain residual foreground. Furthermore, some H I signal will be removed, typically on larger scales where modes are most degenerate with the spectrally smooth foregrounds. We aim to reconstruct this lost signal with a foreground transfer function, which we discuss in Section 4.3.

4.1 Reconvolution of maps

It is understood that a frequency-dependent beam size can cause the foregrounds to leak into a greater number of spectral modes, requiring more aggressive cleaning (Alonso et al. 2015; Switzer et al. 2015). A way to potentially mitigate this issue is to convolve all maps to a common resolution before performing the foreground clean, as done in previous experiments (Masui et al. 2013; Wolz et al. 2017, W22; Anderson et al. 2018). However, recent tests on simulations suggest that a simple Gaussian resmoothing of the data to a common resolution does not improve blind foreground removal techniques, even if the true beam is a perfect Gaussian (Matshawule et al. 2021; Spinelli et al. 2021). For real data though, it is beneficial to resmooth to homogenize some of the systematic contributions from e.g. residual RFI or polarization leakage. For this reason we perform a weighted resmoothing on the *MeerKAT* H I intensity maps prior to foreground cleaning.

An intensity map δT which has a frequency-dependent beam (denoted by the $'$ index) with a FWHM $\theta_{\text{FWHM}}(\nu)$ in degrees, and an angular separation between pixels given by $\Delta\theta$, is convolved with the following kernel:

$$K(\Delta\theta, \nu) = \exp\left[-\frac{\Delta\theta^2}{2[\gamma\sigma_{\text{max}}^2 - \sigma^2(\nu)]}\right], \quad (16)$$

⁴The cross-correlation coefficient r only enters on cross-correlation between biased density terms.

where $\sigma(\nu) = \theta_{\text{FWHM}}(\nu)/(2\sqrt{2\ln 2})$, σ_{max} is the maximum $\sigma(\nu)$ value, and γ is a scaling factor which governs how much the final effective resolution is decreased by.

In previous *Green Bank Telescope (GBT)* studies, a choice of $\gamma = 1.4$ was used (Masui et al. 2013). In this work, due to the already large *MeerKAT* beam, we use a smaller value of $\gamma = 1.2$. We experiment with this choice, and discuss the consequences of varying γ in our results (Section 5). The choice of $\gamma = 1.2$ gives a frequency-independent effective beam size of $\gamma\theta_{\text{FWHM}}(\nu_{\text{min}}) = 1.82$ deg.

The kernel in equation (16) is normalized such that the sum over all pixels is equal to unity, then the weighted convolution used to resmooth the maps is given by

$$\delta T(\theta, \nu) = \frac{[\delta T'(\theta, \nu) w'_{\text{H1}}(\theta, \nu)] * K(\Delta\theta, \nu)}{w'_{\text{H1}}(\theta, \nu) * K(\Delta\theta, \nu)}, \quad (17)$$

where $w'_{\text{H1}}(\theta)$ is the inverse-variance weight. The $*$ denotes a convolution performed separately in each frequency channel e.g. $w'_{\text{H1}}(\theta) * K(\Delta\theta) = \sum_i w'_{\text{H1}}(\theta_i) K(\theta - \theta_i)$, where the summation is over each pixel i . To ensure the weight field still represents the inverse variance of the new resmoothed field, the weight w'_{H1} is convolved according to

$$w_{\text{H1}}(\theta, \nu) = \frac{[w'_{\text{H1}}(\theta, \nu) * K(\Delta\theta, \nu)]^2}{w'_{\text{H1}}(\theta, \nu) * K^2(\Delta\theta, \nu)}. \quad (18)$$

4.2 PCA foreground cleaning

In this work, a PCA-based blind foreground subtraction method is used. The observed intensity maps can be represented by a matrix \mathbf{X}_{obs} with dimensions $N_\nu \times N_\theta$ where N_ν is the number of frequency channels along the line-of-sight and N_θ is the number of pixels. The assumption behind blind-foreground cleaning is that the data can be represented by the linear system $\mathbf{X}_{\text{obs}} = \hat{\mathbf{A}}\mathbf{S} + \mathbf{R}$, where $\hat{\mathbf{A}}$ represents the mixing matrix and \mathbf{S} are the N_{fg} separable source maps identified by projecting the mixing matrix along the data $\mathbf{S} = \hat{\mathbf{A}}^T \mathbf{X}_{\text{obs}}$. In PCA, the mixing matrix is extracted from the eigen-decomposition of the frequency covariance matrix of the mean-centred data, defined by $\mathbf{C} = (\mathbf{w}\mathbf{X}_{\text{obs}})^T (\mathbf{w}\mathbf{X}_{\text{obs}}) / (N_\theta - 1)$, where \mathbf{w} are the inverse variance weights recast into $N_\nu \times N_\theta$ matrices. The eigen-decomposition is then given as $\mathbf{C}\mathbf{V} = \mathbf{V}\mathbf{\Lambda}$, where $\mathbf{\Lambda}$ is the diagonal matrix of eigenvalues ordered by descending magnitude, and \mathbf{V} is the eigenvector, the first N_{fg} of which supplies the set of functions used to construct the mixing matrix. We assume the subtraction of $\hat{\mathbf{A}}\mathbf{S}$ in the linear system will remove dominant foregrounds, leaving behind in the residuals \mathbf{R} most of the HI signal not removed in the subtraction along with Gaussian thermal noise.

We show some resulting maps from the foreground cleaning in Fig. 2. The top panel, which shows the average through frequency, reveals evidence of residual foreground structure which can be seen from comparison with the uncleaned sky map in Fig. 1. However, the amplitude of the map has decreased by several orders of magnitude, thus the foreground residuals should dominate less over the HI fluctuations. The reason for the very low amplitude in the top panel is due to the average through frequency being suppressed in the PCA clean. Since this will remove large radial modes it can conceptually be seen as removing the mean from the line-of-sight. The middle three panels show some examples of cleaned maps in individual frequency channels. Here the amplitude is not as suppressed; however, there is less evidence of residual foreground structure and these maps are more likely dominated by frequency-varying systematics or residual RFI. This is more pronounced in the edges of the map which receive less observation time and are thus down-weighted, as shown by the

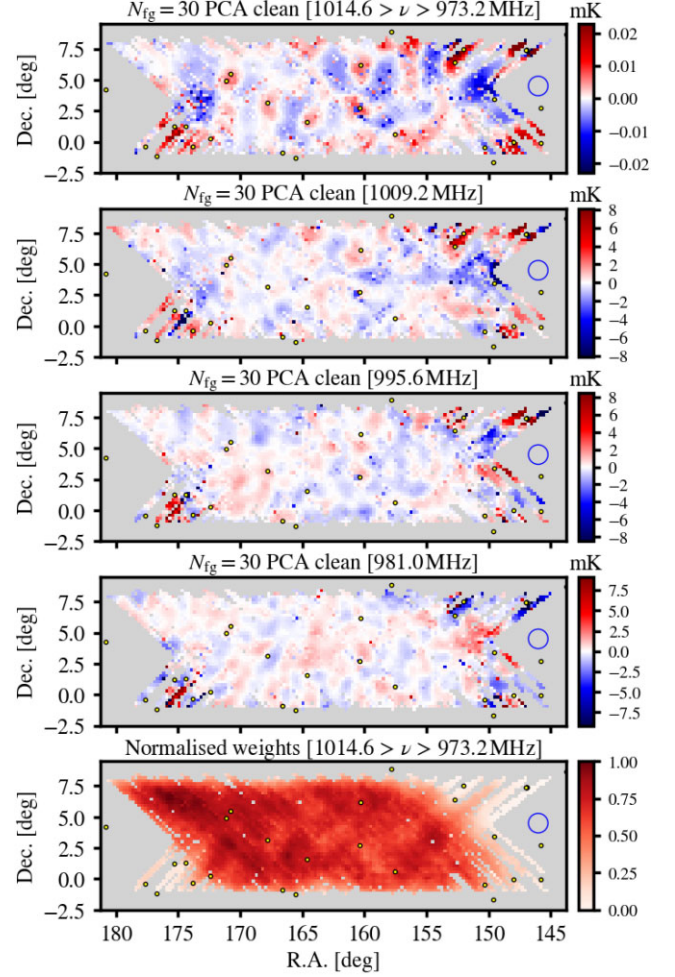


Figure 2. *MeerKAT* intensity maps foreground cleaned by removing $N_{\text{fg}} = 30$ PCA modes. Top panel has been averaged over the 199 frequency channels covering $1014.6 > \nu > 973.2$ MHz ($0.400 < z < 0.459$) (foreground clean performed before averaging through frequency). Middle three panels show some example single frequency channels. Bottom panel shows the normalized weights w_{H1} used in the analysis. The yellow dots show the position of point sources with flux > 1 Jy at 1400 MHz. The blue ring shows the FWHM of the *MeerKAT* beam at the minimum frequency, multiplied by the resmoothing parameter i.e. $\gamma\theta_{\text{FWHM}}(\nu_{\text{min}})$.

bottom panel which presents the normalized weights, w_{H1} , used in this analysis (see Section 2).

4.3 Foreground removal transfer function

We compensate the signal loss due to the foreground cleaning with a transfer function. Following previous literature (Masui et al. 2013; Switzer et al. 2013, 2015), the transfer function can be constructed by injecting mock intensity mapping data \mathbf{M}_{H1} into the true observed data \mathbf{X}_{obs} , which includes foregrounds and observational systematics. By running a PCA clean on this combination, we can measure (and compensate for) the signal loss in the cleaned mock data:

$$\mathbf{M}_{\text{c}} = [\mathbf{M}_{\text{H1}} + \mathbf{X}_{\text{obs}}]_{\text{PCA}} - [\mathbf{X}_{\text{obs}}]_{\text{PCA}}. \quad (19)$$

The $[\]_{\text{PCA}}$ notation represents performing the PCA clean (outlined in Section 4.2) on the quantities inside the brackets, treating them as a single combination. For example, the mixing matrix is not determined separately for both mock and data in $[\mathbf{M}_{\text{H1}} + \mathbf{X}_{\text{obs}}]_{\text{PCA}}$,

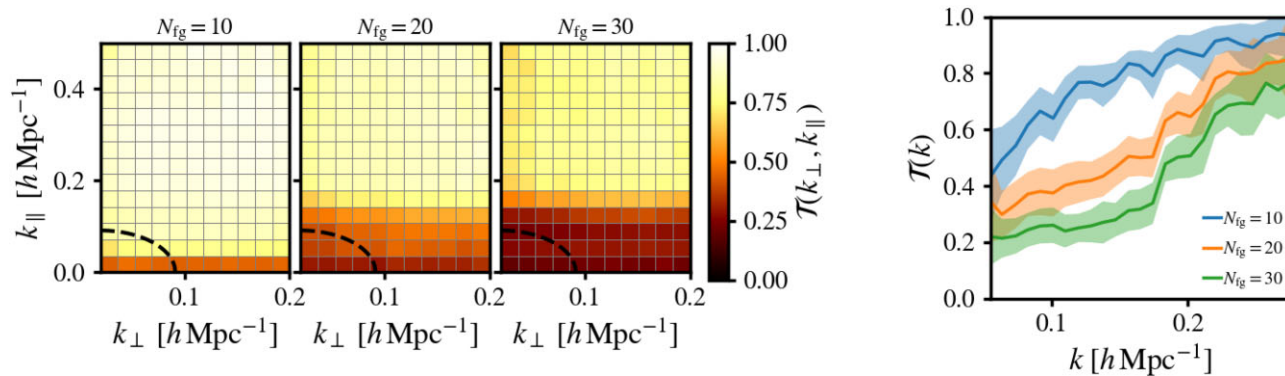


Figure 3. Foreground transfer functions used to correct for the signal loss in the power spectrum measurement from foreground cleaning. A value of $\mathcal{T} = 1$ denotes no signal loss, while $\mathcal{T} \ll 1$ denotes severe signal loss. Three left-hand panels show the transfer function decomposed into k_{\perp} and k_{\parallel} modes for different foreground cleans indicated by N_{fg} . The black-dashed line marks a characteristic scale of $|k| = 0.08 h \text{ Mpc}^{-1}$ (approximately the scale of the first Baryon Acoustic Oscillation (BAO) wiggle maximum). Far-right panel shows the transfer function binned into the same spherically averaged k -bins as those used for the main power spectrum estimation. The shaded regions indicate the 1σ errors estimated from the variance in the 100 simulations used in the construction of $\mathcal{T}(k)$.

but determined for the combination of $\mathbf{M}_{\text{HI}} + \mathbf{X}_{\text{obs}}$. We also subtract the PCA clean of the data, $[\mathbf{X}_{\text{obs}}]_{\text{PCA}}$, since this only adds uncorrelated variance, thus subtracting it makes convergence to a smooth transfer function more efficient, requiring fewer mock iterations. After calculating \mathbf{M}_{c} , we measure the cross-power spectrum with a corresponding mock galaxy map \mathbf{M}_{g} , then divide this by a foreground-free equivalent to estimate the signal loss at each mode:

$$\mathcal{T}(k) = \left\langle \frac{\mathcal{P}(\mathbf{M}_{\text{c}}, \mathbf{M}_{\text{g}})}{\mathcal{P}(\mathbf{M}_{\text{HI}}, \mathbf{M}_{\text{g}})} \right\rangle. \quad (20)$$

$\mathcal{P}()$ denotes an operator which measures the cross-power spectrum, then spherically averages modes into the same k -bins as the data. The angled brackets represent an ensemble average over a large number of mocks (we use 100 in this work).

The HI mocks are generated with the lognormal method (Coles & Jones 1991), sampled from a model HI power spectrum (the same as that used in the power spectrum fitting; see Section 3.2) with a Gaussian smoothing applied perpendicular to the line-of-sight to approximately emulate the *MeerKAT* beam. Similarly, for the galaxy mocks, we generate a lognormal density field with the same random seed as the HI, then Poisson sample galaxies on to the field with the same number count as the WiggleZ catalogue. These steps ensure the mock fields emulate the amplitudes of real maps as realistically as possible. There is evidence suggesting the transfer function is not overly sensitive to the choice of fiducial cosmology (Cunnington 2022); however, further investigation into how much it can be relied on for precision cosmology is required.

We plot the Fourier-space transfer function $\mathcal{T}(k_{\perp}, k_{\parallel})$ in Fig. 3 (three left-hand panels) decomposed into anisotropic k -bins perpendicular ($k_{\perp} = \sqrt{k_x^2 + k_y^2}$) and parallel ($k_{\parallel} \equiv k_z$) to the line-of-sight, as well as $\mathcal{T}(k)$ (far-right panel). As the $\mathcal{T} < 1$ values show, the foreground cleaning is causing signal loss, mostly in the small- k_{\parallel} modes.

Any power spectrum measurement we make on the data is divided by $\mathcal{T}(k)$ to correct for the signal loss (unless clearly stated in demonstrative figures). For the HI autopower spectrum used in the error estimation (outlined in Section 3.1), we also multiply through by $1/\mathcal{T}(k)$. Previous studies have opted to use $1/\mathcal{T}(k)^2$ as a correction instead (Switzer et al. 2013), motivated by the assumption that in autocorrelation, signal loss occurs in both maps, so there should be twice the reconstruction of power needed. However, from simulation

tests, we found this overcorrected the signal loss. Furthermore, our analytical error estimation on the cross-power spectrum, which uses the auto-HI power spectrum, is found to be in good agreement with other approaches of error estimation using the WiggleZ randoms and jack-knife tests. χ^2_{dof} analysis also suggests our errors are not overestimated in any case. This changes if we opt for the $1/\mathcal{T}(k)^2$ correction where it becomes clear that the errors have been overestimated, suggesting that the signal loss in the auto-HI power spectrum has been overcorrected. We defer further investigation into signal loss in the HI autocorrelation to future work.

5 RESULTS

Here, the main results are presented beginning with an analysis of the HI autocorrelation power spectrum (Section 5.1) to provide some insight into the quality of the *MeerKAT* pilot intensity mapping data and the foreground cleaning performance. The main results from the cross-correlation with WiggleZ galaxies are then presented and analysed in Section 5.2 and lastly we provide some constraints on the HI density parameter in Section 5.3.

5.1 HI autopower spectrum

The autopower spectrum of the cleaned HI intensity maps gives some indication of how much foregrounds have been suppressed. In Fig. 4, we show the 2D auto-HI power spectrum. The far-left panel shows the original data before foreground removal, demonstrating the dominance of the foregrounds and their concentration on the largest scales, particularly at small- k_{\parallel} . Removing just a few principal components reduces the amplitude of the autopower spectrum by several orders of magnitude, as shown in the second panel. In simulation tests using foreground models extrapolated from real data, removing $N_{\text{fg}} \sim 4$ PCA modes is sufficient to remove the majority of the foregrounds (Alonso et al. 2015; Cunnington et al. 2021), and this should also be the case for a perfectly designed and calibrated experiment. The resulting cleaned maps in this idealized case would contain HI signal and Gaussian thermal noise, similar to the model in the fifth panel of Fig. 4. The thermal noise in the ideal model is large due to the survey's low observing time. This yields an autopower spectrum amplitude of $P_{\text{noise}} \sim 85 \text{ mK}^2 h^{-3} \text{ Mpc}^3$.

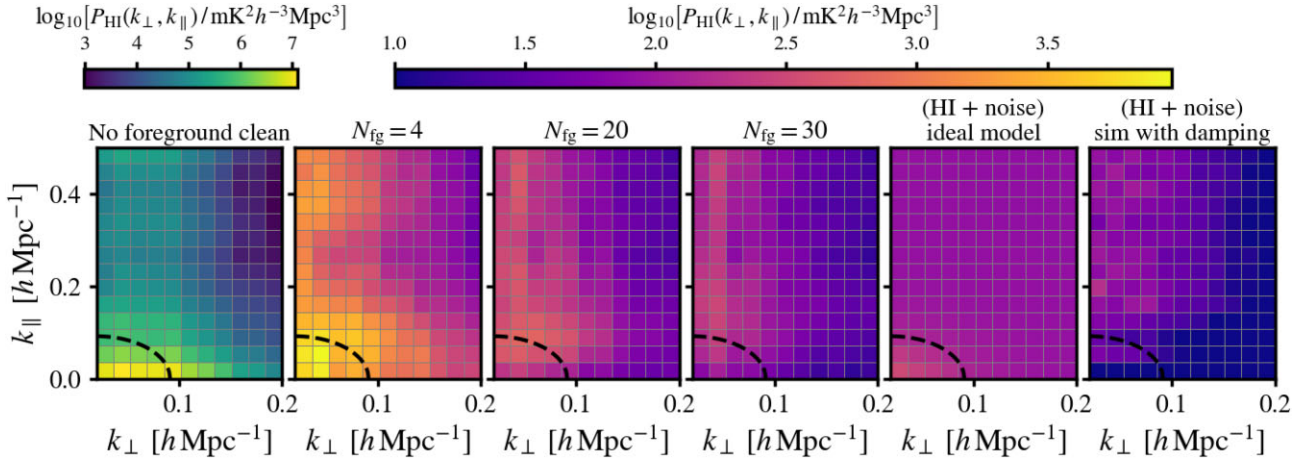


Figure 4. *MeerKAT* HI autopower spectra at $0.400 < z < 0.459$ decomposed into k_{\perp} and k_{\parallel} modes for different foreground cleans indicated by N_{fg} (the number of PCA modes removed). The fifth panel shows a predicted level for the HI signal plus purely Gaussian thermal noise, in an ideal case assuming no signal loss. The thermal noise is predicted to be ~ 2 mK for this survey (estimated in W21). The far-right panel shows a simulation of HI plus Gaussian noise including signal damping from the beam, additional resmoothing and foreground cleaning. As in Fig. 3, the black-dashed line marks a characteristic scale of $|k| = 0.08 h \text{ Mpc}^{-1}$ (approximately the scale of the first BAO wiggle maximum) at which, from our modelling, we would expect the HI power to be $P_{\text{HI}} \sim 100 \text{ mK}^2 h^{-3} \text{ Mpc}^3$, i.e. $\log_{10}[P_{\text{HI}}] = 2$. None of these power spectra have had signal loss reconstructed by the transfer function.

The amplitude of the HI signal varies with scale but should reach⁵ $P_{\text{HI}} \sim 100 \text{ mK}^2 h^{-3} \text{ Mpc}^3$ at around $k \sim 0.08 h \text{ Mpc}^{-1}$ and fall to $P_{\text{HI}} \sim 10 \text{ mK}^2 h^{-3} \text{ Mpc}^3$ at $k \sim 0.18 h \text{ Mpc}^{-1}$, therefore we expect the noise to dominate over the HI signal on most scales, as seen in the Fig. 4 model.

For this pilot-survey data, instrumental calibration imperfections, residual RFI, and other systematics (see discussions in Irfan et al. 2022) will distort the idealized model in Fig. 4. The instrumental response modulates the foregrounds, resulting in additional spectral structure that requires more PCA modes to be removed. Uncleaned modes containing residual foregrounds, RFI, and other systematics will positively bias the autopower spectrum.⁶ This is why for the $N_{\text{fg}} = 4$ case, the power spectrum does not reach the level of the HI signal plus noise.

As N_{fg} increases in Fig. 4, the amplitude of the power drops, and this occurs more severely for large modes, particularly at small- k_{\parallel} . Note we do not correct for signal loss with the transfer function in any of the autopower spectra in Fig. 4 to allow for a more detailed examination. While it appears that the power spectrum is reaching below the idealized HI + noise model at high k_{\perp} and low k_{\parallel} in the $N_{\text{fg}} \geq 20$ cases, a detailed comparison would need to account for the effects of the map reconvolution and the foreground clean, both of which would damp the HI + noise model further. In the far-right panel we show a simulated HI mock with the same noise level as the idealized model, but include some observational effects. To emulate the beam and reconvolution, we smooth the simulation perpendicular to the line-of-sight. We also emulate signal loss from the foreground clean by projecting out modes based on the same PCA mixing matrix functions derived for the $N_{\text{fg}} = 30$ data case. Comparison between the $N_{\text{fg}} = 30$ and far-right panel suggests the measured autopower spectrum from the data has not reached this estimated level, indicating that residual RFI, foregrounds, and other systematics are present in the data. As supported by the foreground

transfer functions in Fig. 3, we know there is signal loss from the foreground clean, hence we are not free to arbitrarily increase the aggressiveness of the foreground clean to further reduce residuals. Thus, a balance is required between reducing foreground residuals and limiting cosmological signal loss.

Since the additive bias from non-cosmological residuals is unknown, it is difficult to compare autocorrelated data and model and conclude that a cosmological detection has been achieved. Cross-correlating with galaxy surveys avoids these additive biases, serving the motivation for this work. We leave a detailed study into the auto-HI power for future work, where we will explore cross-correlating different sets of dishes or observational time blocks [a method adopted in *GBT* experiments (Masui et al. 2013)].

5.2 Cross-correlation with WiggleZ galaxies

There are 4031 galaxies in the overlapping 11 h field of the WiggleZ galaxy survey (Drinkwater et al. 2010, 2018). Following the steps outlined in Section 3.1, we compute an estimate for the cross-power spectrum between the WiggleZ galaxies and the *MeerKAT* intensity maps, foreground cleaned by removing $N_{\text{fg}} = 30$ PCA modes. We present this power spectrum in Fig. 5. The middle panel shows the S/N ratio, where we find $S/N \sim 2$ on large scales. We use an analytical method to estimate the errors (discussed in Section 3.1). At smaller scales, the *MeerKAT* beam (Asad et al. 2021; de Villiers & Cotton 2022), which is significantly larger than previous intensity mapping surveys⁷ (Masui et al. 2013; Anderson et al. 2018; Chakraborty et al. 2021; CHIME Collaboration et al. 2022), is the main reason for the poor S/N , since the signal is damped by the beam.

The model (black-dotted line) in Fig. 5 is calculated following Section 3.2. In this model, we fix all parameters to fiducial quantities except for the degenerate quantity $\bar{T}_{\text{HI}} b_{\text{HI}r}$ for which we assume

⁵We assume $\Omega_{\text{HI}} b_{\text{HI}} = 0.85 \times 10^{-3}$ for the HI model and simulation in Fig. 4.

⁶This assumes these systematics have not caused the gain to be systematically overestimated.

⁷The FWHM for the central lobe of the *MeerKAT* beam is 1.82 deg after resmoothing (see Sections 2 and 4.1). For comparison, this is ~ 4 times larger than the *GBT* (100 m dish diameter) observations at $z \sim 0.8$, who had an effective resolution after resmoothing of $\gamma \theta_{\text{FWHM}} \sim 0.44$ deg using $\gamma = 1.4$ (Masui et al. 2013).

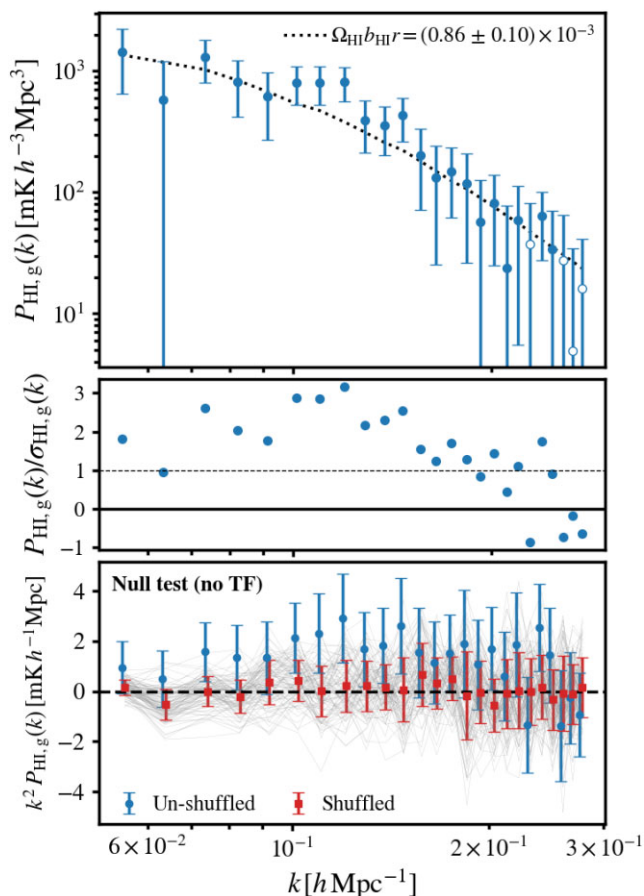


Figure 5. Cross-power spectrum between WiggleZ galaxies and *MeerKAT* HI intensity maps cleaned by removing $N_{\text{fg}}=30$ PCA modes at $0.400 < z < 0.459$, with 1σ error bars (top panel). Hollow markers indicate a negative correlation. The black-dotted line represents a theoretical model (see equation 12), fitted with an amplitude parameter $\Omega_{\text{HI}}b_{\text{HI}}r$ given in the top-right panel. Calculating the $\Delta\chi^2$ relative to a null-model ($P_{\text{HI},g}=0$) evaluates this as a 7.7σ cross-correlation detection. The middle panel shows the ratio between data and error. The bottom panel shows a null test where the WiggleZ galaxy maps have had been shuffled along redshift. The thin grey lines show 100 different shuffles. The average (red squares) and standard deviation (red error bars) across the shuffled samples are shown relative to the original (blue-dots). In both cases in the bottom panel, no scaling by the transfer function has been applied.

scale-independence, hence this quantity will only affect the amplitude of the model. Thus, by fitting the amplitude of the cross-power spectrum, we are sensitive to $\Omega_{\text{HI}}b_{\text{HI}}r$ (from the relation in equation 15). We quote the best-fitting value for $\Omega_{\text{HI}}b_{\text{HI}}r$ in the top-right panel of Fig. 5, which was fitted to the data using a least-squares method. We discuss the parameter constraints on Ω_{HI} in the following section.

We find a good agreement ($\chi_{\text{dof}}^2 \sim 1$)⁸ between the data and model across all scales ($0.05 < k < 0.28 h \text{ Mpc}^{-1}$) in Fig. 5. Furthermore, we analyse $\sqrt{\Delta\chi^2} \equiv \sqrt{\chi^2 - \chi_{\text{null}}^2}$, the difference between the data's χ^2 evaluated using our cross-correlation model, and one using a null model with zero cross-power. This quantifies the statistical significance of the cross-correlation detection. We achieve a 7.7σ

⁸ $\chi_{\text{dof}}^2 \equiv \chi^2/\text{dof}$ where $\text{dof}=24$ are the degrees of freedom which is the number of k -bins minus 1 for the single parameter we fit.

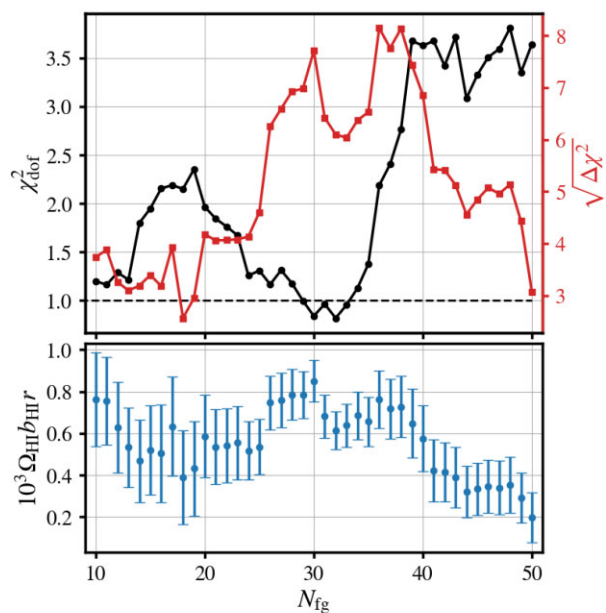


Figure 6. Sensitivity of results to foreground cleaning. Top panel, left-axis, and black-dot data show the reduced χ^2 for each foreground cleaned cross-power spectra relative to its best-fitting model. Top panel, right-axis, and red-square data show the detection significance for the cross-power spectra relative to a null model. Bottom panel shows the variation in the best-fitting $\Omega_{\text{HI}}b_{\text{HI}}r$ for each N_{fg} case, from a least-squares fit to the cross-power spectrum amplitude.

detection, providing strong evidence for the first verification of a cosmological signal with a multidish array performing single-dish intensity mapping.

We conducted various null tests on the analysis pipeline. The bottom panel of Fig. 5 shows the results from shuffling the galaxy maps along the line-of-sight, which should destroy the cross-correlation clustering signal. We re-ran the power spectrum estimation pipeline after each shuffle and found a result consistent with zero. We found similar null results when shuffling the cleaned HI intensity maps along the line-of-sight and swapping the WiggleZ maps with random mocks from Blake et al. (2010).

We did not apply the transfer function in the bottom panel of Fig. 5, since scaling the null results would make no difference. Encouragingly, we were still able to obtain a detection for the original unshuffled results where a transfer function has also not been used. This provides a $> 4\sigma$ detection, which is strong evidence for correlated clustering since this result relied on no signal reconstruction. However, using the transfer function avoids biasing parameter estimates and improves the cross-correlation detection. We therefore implement it in the cross-correlation results.

We experimented with the choice of the resmoothing parameter γ (Section 4.1), finding $\gamma = 1$ produced a noisier power spectrum with worse model agreement. The higher choice of $\gamma = 1.4$ delivered a similarly good model agreement compared to $\gamma = 1.2$, but had a slightly lower cross-correlation detection significance due to the increased damping at high- k . Not performing any deconvolution still delivered a clear detection but resulted in a particularly noisy power spectrum at small- k , indicating the presence of residual foreground and systematics which are mitigated by this resmoothing procedure.

For the power spectrum in Fig. 5 we chose $N_{\text{fg}} = 30$ as it provides an excellent goodness-of-fit (χ_{dof}^2). Fig. 6 (top panel) shows how

varying N_{fig} influences χ_{dof}^2 , which should ideally be close to unity to represent a good model fit to the data with reasonably sized errors. For each N_{fig} case we recalculate the transfer function and re-fit the free parameter $\Omega_{\text{HI}}b_{\text{HI}}r$ (values shown by the bottom panel), which avoids the χ_{dof}^2 improving simply because the amplitude of the power is decreasing into agreement with a pre-selected fiducial $\Omega_{\text{HI}}b_{\text{HI}}r$. We also show the cross-correlation detection strength, given by $\sqrt{\Delta\chi^2}$, on the right-hand (red) axis of Fig. 6 (top panel).

At low N_{fig} , the χ_{dof}^2 appears reasonable; however, this is due to the larger statistical errors on the cross-power spectrum, which is fairly consistent with zero for these N_{fig} , as identified by the low detection significance in the $\sqrt{\Delta\chi^2}$ results. The errors are larger for low N_{fig} because the residual foregrounds contribute significantly more variance to the maps, even though the residuals themselves are expected to correlate out on average. Increasing N_{fig} from 10 to 20 does little to improve the detection significance and initially worsens the χ_{dof}^2 caused by a decrease in error-bar size. At $N_{\text{fig}} \sim 30$ enough components have been removed that a clear detection starts to manifest along with an improved agreement between data and model, given by the $\chi_{\text{dof}}^2 \sim 1$. Going to much higher N_{fig} starts to overclean the maps, reducing S/N and worsening the detection. To justify this explanation for the deterioration in results for $N_{\text{fig}} > 30$, we analysed the cross-correlation for maps constructed using just the principal components between 30 and 40. These maps provided a $\sim 3.4\sigma$ detection, indicating that a lot of signal is present in the modes with $30 < N_{\text{fig}} < 40$, which explains the deterioration in χ_{dof}^2 beyond $N_{\text{fig}} = 30$, where these modes are gradually removed.

The main result we chose to present ($N_{\text{fig}} = 30$) is picked from a region where N_{fig} could be ± 4 of this choice and still deliver a $> 6\sigma$ detection, thus representing robust evidence for cross-correlation. The choice of $N_{\text{fig}} = 30$ offers a good balance between goodness-of-fit (χ_{dof}^2) and detection significance ($\sqrt{\Delta\chi^2}$), as well as a compromise between reducing residual foregrounds and limiting signal loss, as discussed in Section 5.1. However, Fig. 6 highlights the sensitivity of results to the foreground clean, and is further evidence that residual foregrounds and systematics are spread throughout the principal components. The ratio between systematics and signal varies among the various components thus some will be more influential on the cross-correlation than others. This causes a variation in the derived parameter $\Omega_{\text{HI}}b_{\text{HI}}r$, shown by the bottom panel of Fig. 6. We estimate a contribution to the error budget of $\Omega_{\text{HI}}b_{\text{HI}}r$ caused by the variance across the different N_{fig} , discussed further in the following section. An even more detailed understanding of the variation in results with N_{fig} , as well as signal loss correction uncertainties, must be gained from end-to-end simulations which we are pursuing for future work.

5.3 Constraints on Ω_{HI}

Fitting the amplitude of the HI-galaxy cross-power spectrum provides a constraint on $\Omega_{\text{HI}}b_{\text{HI}}r$ as a function of redshift. From our results in Fig. 5, we find $\Omega_{\text{HI}}b_{\text{HI}}r = [0.86 \pm 0.10 (\text{stat}) \pm 0.12 (\text{sys})] \times 10^{-3}$. The systematic error accounts for uncertainty from the map calibration and variance in results from the choice of N_{fig} . Firstly, uncertainty from the map calibration could cause a bias to the overall amplitude of the power spectrum. We address this by studying the residuals relative to the model in our calibration study (W21). We are able to estimate that gain uncertainties should be at a level of ~ 2 per cent. Secondly, we account for the variance in results from the different number of PCA modes removed, indicative of residual systematics. We do this by evaluating the standard deviation on all $\Omega_{\text{HI}}b_{\text{HI}}r$ fits (see Fig. 6,

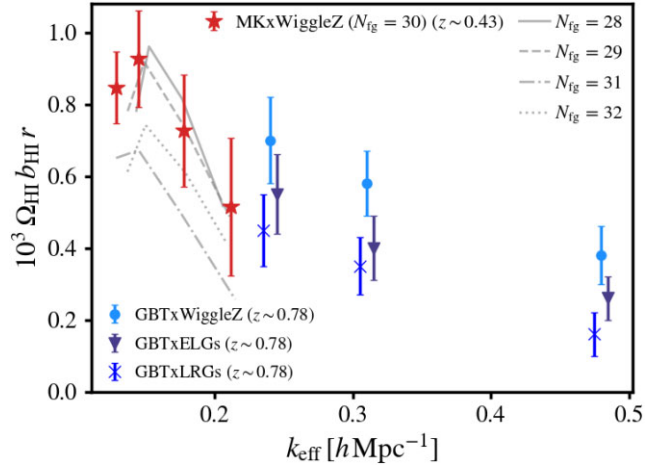


Figure 7. Constraints on $\Omega_{\text{HI}}b_{\text{HI}}r$ measured at different effective scales k_{eff} , achieved by removing low- k data points from the cross-power spectrum, the data-points for each case are therefore not independent. The results for this paper are shown in red-stars using an $N_{\text{fig}} = 30$ PCA clean and the four grey lines show results from different values of N_{fig} . For comparison we also plot the recent results from *GBT* cross-correlations (W22).

bottom panel) from each reasonable choice of N_{fig} ($10 < N_{\text{fig}} < 40$), which we find to be ~ 0.115 , equating to ~ 13 per cent error on $\Omega_{\text{HI}}b_{\text{HI}}r$. The combination of these two error components added in quadrature yields the systematic error in our final constraint.

The HI bias is not yet well understood but is expected to have some scale-dependence when entering non-linear scales (high- k , Carucci et al. 2015; Villaescusa-Navarro et al. 2018; Spinelli et al. 2020). Furthermore, the cross-correlation coefficient r , included to account for stochasticity between the two fields, will also have some scale-dependence. We therefore examined how the constraint on $\Omega_{\text{HI}}b_{\text{HI}}r$ changed as we varied the scales at which it was measured. By removing small- k data points, we change the effective scale of the measurement, calculated by

$$k_{\text{eff}} = \frac{\sum_i k_i (S/N)_i^2}{\sum_i (S/N)_i^2}, \quad (21)$$

where $(S/N)_i$ is the S/N ratio in each k_i bin, i.e. $\hat{P}_{\text{HI,g}}(k_i)/\hat{\sigma}_{\text{HI,g}}(k_i)$. The scale-dependence on the measurements of $\Omega_{\text{HI}}b_{\text{HI}}r$ is shown in Fig. 7 (red-star points) for $N_{\text{fig}} = 30$. The other coloured data points show previous intensity mapping constraints from *GBT* cross-correlation with galaxy surveys at $z \sim 0.8$ (W22). The *GBT* intensity maps had a significantly smaller beam than *MeerKAT* thus were able to probe higher- k . The *MeerKAT* and *GBT* measurements are at different redshifts so a direct comparison is not possible. Despite this, there still appears to be a trend with k_{eff} suggesting a detection of scale-dependence in $b_{\text{HI}}r$. However, the continuity of the trend is affected by the choice of N_{fig} , as shown by the different grey lines in Fig. 7. Furthermore, there is a possibility the scale-dependence is influenced by systematics, which are mitigated in the scale cuts. The smallest- k modes are the most affected by the transfer function, with up to 80 per cent increase in amplitude (see Fig. 3). Thus, further investigation is needed to disentangle the scale-dependence of $b_{\text{HI}}r$ from possible scale-dependent systematics. Despite using the same scale cuts in Fig. 7 for each N_{fig} case, the effective scale is recalculated each time according to equation (21) and can therefore provide different k_{eff} which explains the slight horizontal offsets in the curves for different N_{fig} .

By making some further assumptions on b_{HI} and r , we can isolate the constraint on Ω_{HI} . The cross-correlation coefficient r is not currently well understood with more observational and simulation-based studies required. It will also vary depending on the HI content of the selected optical galaxies (Wolz et al. 2016). However, on large scale it is reasonable to assume r should be close to unity and reasonably independent of redshift. For our purposes, we therefore assume $r = 0.9 \pm 0.1$ (Khandai et al. 2011) and for the bias we interpolate between the hydrodynamic simulations in Villaescusa-Navarro et al. (2018) and use $b_{\text{HI}} = 1.13 \pm 0.10$. Fitting the power spectrum data in Fig. 5 across all scales ($k_{\text{eff}} \sim 0.13 h \text{ Mpc}^{-1}$), provides a constraint of $\Omega_{\text{HI}} = [0.83 \pm 0.15 (\text{stat}) \pm 0.11 (\text{sys})] \times 10^{-3}$ at the redshift of $z = 0.43$, which is reasonably consistent with other results in the literature (see comparison in W22).

6 CONCLUSION

HI intensity mapping is a novel method for probing large-scale cosmic structure and will be a primary objective for the future SKAO. To achieve this, it is necessary for the multidish array to operate in single-dish (autocorrelation) mode, as opposed to a conventional interferometer. In this work we have demonstrated, for the first time, the successful detection of cosmological signal using the MeerKAT multidish array in single-dish mode. This represents a major milestone in demonstrating the feasibility of this survey mode for SKAO.

We achieved this by cross-correlating 10.5 h of MeerKAT pilot survey intensity maps with overlapping optical galaxies from the WiggleZ Dark Energy Survey. A measurement of the cross-power spectrum between these fields provided a 7.7σ detection of a cross-correlation. We relied on an aggressive filtering process, removing 30 modes in a PCA-based foreground clean, necessary due to the presence of systematic contributions in the pilot survey data. This allowed us to obtain a constraint of $\Omega_{\text{HI}} b_{\text{HI}} r = [0.86 \pm 0.10 (\text{stat}) \pm 0.12 (\text{sys})] \times 10^{-3}$ from fitting the amplitude of the cross-power spectrum at an effective scale of $k_{\text{eff}} \sim 0.13 h \text{ Mpc}^{-1}$. Varying the effective scale of the measurement changed the value for $\Omega_{\text{HI}} b_{\text{HI}} r$, something noted in previous studies (W22). We also found $\Omega_{\text{HI}} b_{\text{HI}} r$ to have a dependence on the number of foreground modes removed, so we included this variance in the systematic error budget of the constraint. The ~ 17.8 per cent precision represents a competitive $\Omega_{\text{HI}} b_{\text{HI}} r$ constraint relative to other intensity mapping experiments. Furthermore, with additional assumptions on b_{HI} and r , we provided insight into the cosmic HI density Ω_{HI} , for which measurements at higher redshifts are vital for understanding the evolution of HI.

The MeerKAT telescope will continue to conduct HI intensity mapping observations in single-dish mode. With enhanced calibration techniques and more observing time, improved constraints will be possible with less aggressive foreground removal. With this we can attempt a detection of the HI in autocorrelation, which is yet to be achieved. Observations have now been conducted in MeerKAT's UHF band ($0.40 < z < 1.45$), opening the possibility of higher redshift probes and for cross-correlating UHF-band data with the L-band data used in this work, with the aim of mitigating systematics.

ACKNOWLEDGEMENTS

The authors would like to thank Stefano Camera for useful comments and questions during the development of this project. We would also like to thank Sourabh Paul for his comments on the final manuscript.

Lastly, we would like to extend our gratitude to the referee whose remarks improved the quality of the final paper.

SC is supported by a UK Research and Innovation Future Leaders Fellowship grant [MR/V026437/1] and also acknowledges funding from the UK Research and Innovation Future Leaders Fellowship grant [MR/S016066/1]. MGS, YL, and JW acknowledge support from the South African Radio Astronomy Observatory and National Research Foundation (Grant No. 84156). IPC acknowledges support from the 'Departments of Excellence 2018-2022' Grant (L. 232/2016) awarded by the Italian Ministry of University and Research (MUR). AP is a UK Research and Innovation Future Leaders Fellow [grant MR/S016066/1]. LW is a UK Research and Innovation Future Leaders Fellow [grant MR/V026437/1]. MS acknowledges support from the AstroSignals Synergia grant CRSII5_193826 from the Swiss National Science Foundation. PS is supported by the Science and Technology Facilities Council [grant number ST/P006760/1] through the DISCnet Centre for Doctoral Training. This result is part of a project that has received funding from the European Research Council (ERC) under the European Union's Horizon 2020 research and innovation programme (Grant agreement No. 948764; PB). PB acknowledges support from STFC Grant ST/T000341/1. JF acknowledges support from the Fundação para a Ciência e a Tecnologia (FCT) through the Investigador FCT Contract No. 2020.02633.CEECIND/CP1631/CT0002 and the research grants UIDB/04434/2020 and UIDP/04434/2020.

We acknowledge the use of the Ilifu cloud computing facility, through the Inter-University Institute for Data Intensive Astronomy (IDIA). The MeerKAT telescope is operated by the South African Radio Astronomy Observatory, which is a facility of the National Research Foundation, an agency of the Department of Science and Innovation.

For the purpose of open access, the author has applied a Creative Commons Attribution (CC BY) licence to any Author Accepted Manuscript version arising.

DATA AVAILABILITY

The data underlying this article will be shared on reasonable request to the corresponding author. Access to the raw data used in the analysis is public (for access information please contact archive@ska.ac.za).

REFERENCES

- Akeret J., Seehars S., Chang C., Monstein C., Amara A., Refregier A., 2017, *Astron. Comput.*, 18, 8
- Alonso D., Bull P., Ferreira P. G., Santos M. G., 2015, *MNRAS*, 447, 400
- Anderson C. J. et al., 2018, *MNRAS*, 476, 3382
- Asad K. M. B. et al., 2021, *MNRAS*, 502, 2970
- Battye R. A., Davies R. D., Weller J., 2004, *MNRAS*, 355, 1339
- Battye R. A., Browne I. W. A., Dickinson C., Heron G., Maffei B., Pourtsidou A., 2013, *MNRAS*, 434, 1239
- Bharadwaj S., Nath B., Nath B. B., Sethi S. K., 2001, *J. Astrophys. Astron.*, 22, 21
- Bigot-Sazy M.-A. et al., 2016, ASP Conf. Ser. Vol. 502, *Frontiers in Radio Astronomy and FAST Early Sciences Symposium 2015*. Astron. Soc. Pac., San Francisco, p. 41
- Blake C., 2019, *MNRAS*, 489, 153
- Blake C. et al., 2010, *MNRAS*, 406, 803
- Blake C. et al., 2011, *MNRAS*, 415, 2876
- Bull P., Ferreira P. G., Patel P., Santos M. G., 2015, *ApJ*, 803, 21
- Carucci I. P., Villaescusa-Navarro F., Viel M., Lapi A., 2015, *J. Cosmol. Astropart. Phys.*, 07, 047

- Chakraborty A. et al., 2021, *ApJ*, 907, L7
- Chang T.-C., Pen U.-L., Peterson J. B., McDonald P., 2008, *Phys. Rev. Lett.*, 100, 091303
- Chang T.-C., Pen U.-L., Bandura K., Peterson J. B., 2010, *Nature*, 466, 463
- CHIME Collaboration et al., 2022, preprint ([arXiv:2202.01242](https://arxiv.org/abs/2202.01242))
- Coles P., Jones B., 1991, *MNRAS*, 248, 1
- Cunnington S., 2022, *MNRAS*, 512, 2408
- Cunnington S., Pourtsidou A., Soares P. S., Blake C., Bacon D., 2020, *MNRAS*, 496, 415
- Cunnington S., Irfan M. O., Carucci I. P., Pourtsidou A., Bobin J., 2021, *MNRAS*, 504, 208
- de Villiers M. S., Cotton W. D., 2022, *AJ*, 163, 135
- Drinkwater M. J. et al., 2010, *MNRAS*, 401, 1429
- Drinkwater M. J. et al., 2018, *MNRAS*, 474, 4151
- Feldman H. A., Kaiser N., Peacock J. A., 1994, *ApJ*, 426, 23
- Irfan M. O. et al., 2022, *MNRAS*, 509, 4923
- Kaiser N., 1987, *MNRAS*, 227, 1
- Khandai N., Sethi S. K., Di Matteo T., Croft R. A. C., Springel V., Jana A., Gardner J. P., 2011, *MNRAS*, 415, 2580
- Lewis A., Challinor A., Lasenby A., 2000, *ApJ*, 538, 473
- Li J. et al., 2020, *Sci. China Phys. Mech. Astron.*, 63, 129862
- Li L., Staveley-Smith L., Rhee J., 2021a, *Res. Astron. Astrophys.*, 21, 030
- Li Y., Santos M. G., Grainge K., Harper S., Wang J., 2021b, *MNRAS*, 501, 4344
- Linder E. V., 2005, *Phys. Rev. D*, 72, 043529
- Masui K. W. et al., 2013, *ApJ*, 763, L20
- Matshawule S. D., Spinelli M., Santos M. G., Ngobese S., 2021, *MNRAS*, 506, 5075
- Newburgh L. B. et al., 2014, Proc. SPIE Conf. Ser. Vol. 9145, Ground-based and Airborne Telescopes V. SPIE, Bellingham, p. 91454V
- Newburgh L. B. et al., 2016, Proc. SPIE Conf. Ser. Vol. 9906, Ground-based and Airborne Telescopes VI. SPIE, Bellingham, p. 99065X
- Norberg P., Baugh C. M., Gaztanaga E., Croton D. J., 2009, *MNRAS*, 396, 19
- Planck Collaboration I, 2020, *A&A*, 641, A1
- Pourtsidou A., Bacon D., Crittenden R., 2017, *MNRAS*, 470, 4251
- PUMA Collaboration et al., 2019, BASS, 51, 53
- Santos M. G. et al., 2017, Proceedings, MeerKAT Science: On the Pathway to the SKA (MeerKAT2016). SISSA, South Africa
- SKA Cosmology SWG, 2020, *Publ. Astron. Soc. Aust.*, 37, e007
- Soares P. S., Cunnington S., Pourtsidou A., Blake C., 2021, *MNRAS*, 502, 2549
- Spinelli M., Zoldan A., De Lucia G., Xie L., Viel M., 2020, *MNRAS*, 493, 5434
- Spinelli M., Carucci I. P., Cunnington S., Harper S. E., Irfan M. O., Fonseca J., Pourtsidou A., Wolz L., 2021, *MNRAS*, 509, 2048
- Switzer E. R. et al., 2013, *MNRAS*, 434, L46
- Switzer E. R., Chang T.-C., Masui K. W., Pen U.-L., Voytek T. C., 2015, *ApJ*, 815, 51
- Tegmark M., 1997, *ApJ*, 480, L87
- Tramonte D., Ma Y.-Z., 2020, *MNRAS*, 498, 5916
- Vanderlinde K. et al., 2019, *Canadian Long Range Plan for Astronomy and Astrophysics White Papers, LRP2020*, [accessed date 9th November 2022]
- Villaescusa-Navarro F. et al., 2018, *ApJ*, 866, 135
- Wang J. et al., 2021, *MNRAS*, 505, 3698 (W21)
- Wolz L., Tonini C., Blake C., Wyithe J. S. B., 2016, *MNRAS*, 458, 3399
- Wolz L. et al., 2017, *MNRAS*, 464, 4938
- Wolz L. et al., 2022, *MNRAS*, 510, 3495 (W22)
- Wuensche C. A., 2019, J. Phys. Conf. Ser., 1269, 012002
- Wyithe S., Loeb A., Geil P., 2008, *MNRAS*, 383, 1195

This paper has been typeset from a $\text{\TeX}/\text{\LaTeX}$ file prepared by the author.